Science Advances NAAAS

Manuscript

FRONT MATTER

3 Title

1 2

4

5

6

- Grain boundary dynamics driven by magnetically induced circulation at the void interface of 2D colloidal crystals
- Magnetically driven grain boundary dynamics

78 Authors

Dana M. Lobmeyer, ¹ Sibani L. Biswal¹*

9 10 11

12

13 14

15 16 17

18

19

20

21

22

23

2425

26

27

28

29

Affiliations

- 1. Department of Chemical and Biomolecular Engineering, Rice University, Houston, TX 77005 USA.
- * Corresponding Author. Email: biswal@rice.edu

Abstract

The complexity of shear-induced grain boundary dynamics has been historically difficult to view at the atomic scale. Meanwhile, 2D colloidal crystals have gained prominence as model systems to easily explore grain boundary dynamics at single particle resolution but have fallen short at exploring these dynamics under shear. Here, we demonstrate how an inherent interfacial shear in 2D colloidal crystals drives microstructural evolution. By assembling paramagnetic particles into polycrystalline sheets using a rotating magnetic field, we generate a particle circulation at the interface of particle-free voids. This circulation shears the crystalline bulk, operating as both a source and sink for grain boundaries. Furthermore, we show that the Read-Shockley theory for hard-condensed matter predicts the misorientation angle and energy of shear-induced low-angle grain boundaries based on their regular defect spacing. Model systems containing shear provide an ideal platform to elucidate shear-induced grain boundary dynamics for use in engineering new/improved materials.

30 31 32

Teaser

Spinning particles, driven by a magnetic field, produce interfacial shear that reorganizes the polycrystalline bulk

343536

33

MAIN TEXT

3738

39

40

41

42

43

44

45

Introduction

Polycrystalline materials such as metals, ceramics, and semiconductors contain planar defects at the interface between crystalline grains. These grain boundaries heavily influence bulk material properties such as electrical conductivity and yield strength. Grain boundary strengthening is one well-known example of this influence, where the yield strength of the material is improved by increasing the density of grain boundaries (1). This structure-property relationship is even more salient in two-dimensional (2D) materials because the reduced dimension causes higher sensitivity to crystalline defects (2,3).

However, this relationship is complicated by the dynamic nature of grain boundaries. Under an external force, grain boundaries can translate, form new, or disappear entirely to accommodate stresses and strains imposed on the bulk material (4). Shear stress, in particular, has been connected with grain boundary motion and grain rotation (5-7). However, despite extensive efforts to understand the interplay of shear and grain boundary motion, much of these shear-induced dynamics are still not well understood.

To better understand atomic scale dynamics, colloidal crystals have been used as experimental, model systems, where individual particle resolution and tracking is easily achieved (8). Colloidal crystal grain boundary studies have predominantly elucidated grain boundary dynamics in self-assembled systems, e.g., observing fluctuations at equilibrium (9-12) or probing the dynamics with a step-like energy input (13-16). However, these self-assembled systems do not provide the appropriate conditions to investigate the influence of a continuous shear at the material interface. While there have been self-assembled colloidal systems that have introduced shear stress through extrinsic means (17-19), grain boundary motion due to a continuous interfacial shear has not been reported.

Here, we report experiments of 2D colloidal polycrystalline sheets containing voids, whereby a rotating magnetic field (RMF) produces shear-induced grain rotation and grain boundary formation. We identify the newly formed grain boundaries as low angle grain boundaries (LAGBs) and apply the Read-Shockley dislocation model for crystal grain boundaries (20) to estimate their energies. This work presents, for the first time, the interfacial dynamics at the solid-vapor interface and the role of shear in directing the microstructure of the colloidal crystalline bulk. Ultimately, our work highlights a novel use of a highly dynamic soft matter system that expands the capabilities of colloidal crystals in understanding solid-state phenomena under interfacial shear.

Results and Discussion

Magnetically formed 2D colloidal sheets

To produce our highly dynamic soft matter system, we employ a magnetic assembly method previously reported by our group (21). The crystalline colloidal sheets used in this study are composed of 1 μ m superparamagnetic spheres (Dynabeads MyOne Carboxylic Acid, Invitrogen) suspended in 10mM NaCl. Following previous work (22), a particle monolayer is achieved by confining the particle suspension between parallel glass plates and particle settling due to gravity. The electrostatic surface charges imparted by the carboxylic functional group prevents particle aggregation and particle-surface sticking, while the suspending fluid screens these charges to allow for compact particle packing.

To assemble the particles into an ordered crystalline sheet, the monolayer is subjected to an in-plane RMF. Under the application of an external magnetic field, superparamagnetic particles acquire induced dipole moments. In static fields, this dipolar interaction is anisotropic, creating chains of particles aligned in the field direction. In RMFs, the dipolar interactions can be time-averaged by implementing sufficiently high rotational frequencies. The result is an isotropic attractive interaction that clusters particles in 2D (23-27). Analogous phenomena can also be created with rotating electric fields (28). In our magnetic system, this time-averaged interaction occurs alongside the electrostatic interaction caused by surface charges. The simultaneous interactions produce a tunable long-range attractive and short-range repulsive interaction pair-potential (Fig. 1A) that is analogous to the Lennard-Jones potential for atomic and molecular systems (29). These interactions are sufficiently modeled by the mutual dipolar model (long-range attraction), where mutual interactions between neighboring particles are incorporated, and the Derjaguin–Landau–Verwey–Overbeek (DLVO) theory (short-range repulsion) that is

suitable for charged colloids (21). The tunable nature of our system lies in the magnetic field strength acting as an effective inverse of temperature that can transition the system through phases (30). In other words, an increase in magnetic field strength transitions a disordered phase to a more ordered one, just as a decrease in temperature in hard-condensed matter transitions a liquid to a solid.

The current study operates at relatively high magnetic field strengths for this system (1.1-1.2 mT) and a rotational frequency of 20 Hz. We previously used a RMF of 20 Hz and a range of field strengths to induce phase separation of particles into particle dense and particle void regions (31). Operating at relatively high field strengths for this work induces hexagonally ordered crystalline sheets that contain particle-free voids (Fig. 1B), analogous to a solid-vapor coexistence. The ubiquity of void formation can be made less by increasing the particle concentration, up until the spherical particle packing surpasses the surface area of the chamber floor and multi-layers form. For this work, we study monolayers and focus on the microstructural effect of the crystal-void interface. It is important to note that the energy imparted by the magnetic field maintains the colloidal assembly, thereby inherently keeping the system at nonequilibrium.

System Evolution

The constant energy input imparted by the rotating magnetic field results in highly dynamic colloidal sheets, whereby crystalline grains change in size and orientation with time. Figure 2 shows the typical time evolution of the crystalline bulk via microscopy images overlaid with a θ_6 colormap and the fraction of particles that constitute grain boundaries, x_{GB} , as a function of time. Particles in grain boundaries are defined as any particle with a $\psi_6 \le 0.4$. Initially, the crystalline bulk presents with many grain boundaries (Fig. 2A). This behavior is typical of colloidal crystal systems formed with self-assembly methods (11). However, our system exhibits significant structural reorganization over the course of a few hours. This reorganization is a direct result of the nonequilibrium nature imparted by the magnetic field.

After the crystalline grains form, the bulk restructures to reduce the number of grain boundaries (Fig. 2, B to D). These changes occur at a much slower timescale compared to the rapid initial formation of crystalline grains. This rate continues to decrease as more grain boundaries disappear, as shown by the rate of decrease in x_{GB} (Fig. 2F). Within the first 20 minutes, the fraction of particles residing in grain boundaries decreases by one percent. Over the next 40 minutes, this fraction only decreases by half a percent more before it begins to level out. Grain boundaries have an excess free energy associated with their interface, so it follows that the system would look to remove grain boundaries in an attempt to reach an energy minimum. Such slowing down of bulk dynamics suggests the system is reaching a quasi-equilibrium, whereby structural rearrangements are not significant. However, the continuous energy input supplied by the RMF results in new grain boundaries appearing at later times (Fig. 2E). This formation is evident in a later increase in x_{GB} .

The voids within the crystalline bulk also evolve. Such voids exhibit coarsening and Oswald ripening, leading some to grow over time and others to disappear (31). This global and microstructural evolution occurs despite much of the system remaining in a hexagonally ordered solid phase. Beyond thermal fluctuations, individual particle movement is confined to the grain boundaries that separate the crystalline grains and the disordered crystal-void interface. Crystal-void interfaces are more dynamic than grain boundaries because of the spatial freedom afforded by the void. These highly dynamic

solid-gas interfaces have the ability to reorganize the nearby bulk, thereby acting as both a source and sink for grain boundaries.

Circulation at Voids

At the void interface, a field-induced particle circulation arises. The circulation occurs in the opposite direction of field rotation, as shown in Fig. 3A, and at a significantly slower frequency compared to that of the applied field. Additionally, this circulation is only a few particles thick and therefore, does not penetrate deep into the bulk (see movie S1). This thin, disordered interface is highlighted in Fig. 3A via an overlaid ψ_6 colormap.

The circulation at the crystal-void interface is a result of individual particle rotation. Superparamagnetic colloids have been shown to rotate at similar frequencies. both as individual particles (32) and small, symmetric, seven particle clusters (33). This rotation has been attributed to a nonuniform magnetic distribution within the particles (34), an internal magnetic relaxation (35), or, in the case of clusters, temporary cluster anisotropy caused by a viscoelastic relaxation. While the source of this rotation is the subject of debate, the rotation of individual particles has been used to translate groups of particles (36,37), and it explains the circulation we observe at our interface. When a particle rotates in a fluid, it produces a circulating flow that will translate the particle if it is brought near a stationary surface. This translation is a result of the frictional shear force produced between the particle's flow field and the surface. Otherwise known as a transverse force, this type of force has implications on structure and transport in collective systems (38-41). In the case of our collective system, the particles rotate parallel to the stationary chamber surface and therefore, produce this frictional shear force with other inplane rotating particles. Within the ordered bulk, this force is balanced due to hexagonal symmetry, but at the interface it is unbalanced, causing particles to translate along the edge.

The circulatory motion induced by individual particle rotation produces a collective interfacial shear. This interfacial shear is similar to clusters of Janus magnetic particles that were shown to exhibit shear-induced rotation as a result of rotation-translation coupling between particles at the interface (42). However, since voids are the structural inverse of clusters, there is no self-contained object to rotate in our system. Instead, the circulation-induced shear force causes local rotation of the nearby crystalline bulk (Fig. 3, B and C) thereby acting as a driving force for structural reorganization. In this way, large voids operate as a source of interfacial shear on the 2D crystalline bulk, a dimensional shear that has been difficult to achieve experimentally.

Voids as sources and sinks for grain boundaries

The interfacial shear at the void reorganizes the crystalline bulk by either annihilating or forming grain boundaries. At early times, voids tend to operate as sinks that annihilate grain boundaries, while at later times, they typically switch to operating as sources that form grain boundaries (Fig. 2). However, whether a void operates as a source, or a sink depends on the local microstructure near the void at that point in time. This is best understood with an energy argument.

The RMF supplies a steady input of energy to the system that maintains the assembly while inducing an interfacial shear force at the voids. This shear force is unbalanced, thereby causing energy to constantly transfer from the void, to and through the crystalline bulk. This propagation of energy is what ultimately alters the microstructure of the crystalline bulk. However, the result of this propagation varies, i.e., annihilation vs formation, and is likely caused by differences in the energy state of the

crystalline bulk relative to the energy imparted by shear at the void. The crystalline bulk starts at its peak polycrystallinity, and therefore its peak energy due to the added energy cost of grain boundaries. While in this relatively high energy state, the interfacial shear at the void acts as a form of agitation that dissipates the bulk's energy through the annihilation of grain boundaries. As time progresses, the decrease in the bulk's energy allows for voids to switch to operating as sources. However, grain boundary formation only occurs if the local energy and microstructure near the void are favorable, e.g., the low energy of a large single crystal bordering a void.

Structurally, the physical phenomenon that allows voids to operate as sources or sinks is the same. The interfacial shear rotates the nearby crystal, and this rotation propagates deep into the crystalline bulk. Figure 4 shows two examples of this rotation, as grain boundary formation (Fig. 4, A to E) and grain boundary annihilation (Fig. 4, F to J). It's important to note that the viewing of the crystalline bulk was prioritized over the voids in these images; therefore, many of the images do not explicitly show the nearby voids, but they are just outside of view. The similar time stamps of formation and annihilation reveal that the length of time the RMF has been on for does not solely dictate which phenomenon occurs. This similar time span emphasizes the importance of the local microstructure in determining whether voids operate as sources or sinks after the system's initial re-organization.

The local rotation induced by shear at the void produces orientational changes in a disorganized fashion initially (Fig. 4, A to B and F), before forming a distinct grain boundary that translates through the bulk (Fig. 4, C to D and G to I). This grain boundary propagation either creates grain boundaries that persist (Fig. 4E) or creates a temporary grain boundary that ultimately merges with an existing one, thereby removing a grain and its grain boundary in the process (Fig. 4J). In both cases, the grain boundary propagation results from grain growth that occurs as the crystalline portion near the void rotates. This mechanism is similar to the phenomenon in hard-condensed matter where stress-induced grain rotation induces grain growth (43).

The newly formed grain boundaries' persistent (formation) and transient (annihilation) nature is reflected in x_{GB} and the probability distribution of θ_6 . In the case of formation, the grain boundary persistence is reflected in an increase in x_{GB} that is maintained with time (Fig. 4K). Furthermore, the measured probability distribution of θ_6 begins to branch out as x_{GB} increases (Fig. 4L). These new branches are also maintained with time and indicate the formation and persistence of new grains. In the case of annihilation, the transient nature of the grain boundary formed by the void is reflected by temporary increases in x_{GB} that do not persist (Fig. 4M). These transient stages are the result of x_{GB} being calculated on a total per frame. This means that any change to grain boundary length and number in the frame of view affects the value of x_{GB} . Therefore, when the new grain boundary formed by the void moves into the frame of view, or an existing grain boundary deforms and lengthens the boundary, x_{GB} temporarily increases. However, the overall trend of x_{GB} is decreasing, emphasizing annihilation. Furthermore, the probability distribution in Fig. 4N for 10° disappears around 108 minutes, emphasizing the removal of the grain.

The direction of crystalline rotation is determined by the direction of the interfacial shear along the void(s). Since the rotating field induces a particle circulation in the opposite direction along the crystal-void interface, the interfacial shear can be made clockwise or counterclockwise, depending on the field direction used. By controlling the direction of particle circulation and therefore, the direction of the shear, the sense of rotation to form a new grain or annihilate an existing one is controllable. In the present

Page 5 of 18

examples, formation occurs in the counterclockwise direction and annihilation occurs in the clockwise direction, but this is not always true. When a void contains a clockwise shear, the nearby crystalline bulk will be rotated in the counterclockwise direction, e.g., Fig. 4 (A to E), as previously shown in Fig. 3C. In contrast, Fig. 4 (F to J) shows the crystalline bulk near several voids that are out of view to the left and above the image that contain counterclockwise shear. This counterclockwise shear rotates the crystalline bulk in the clockwise direction. In other words, the crystalline bulk is rotated in the direction of the RMF. While shear is known to be capable of annihilating and/or forming grain boundaries, such a phenomenon as a result of inherent, controllable interfacial shear has not been reported in 2D colloidal crystals prior to this work.

Structure of shear-induced LAGBs

42.

The grain boundaries formed by the shear-induced rotation are low angle grain boundaries (LAGBs), characterized by a small misorientation angle θ_{mis} . The misorientation angle quantifies the orientational difference between neighboring grains and is typically less than 15 degrees for LAGBs (44). Figure 5A depicts a typical LAGB where θ_{mis} is approximately 7°. While the boundary of this LAGB is clearly defined with the θ_6 colormap, a ψ_6 colormap reveals isolated points of disorder that follow the boundary, rather than a complete boundary of disorder (Fig. 5B). The isolated points of disorder are known as dislocations. Grain boundaries consisting of regularly spaced dislocations are typical of LAGBs in hard-condensed (45,46) and soft (13,47) matter, whereas high angle grain boundaries (HAGBs) usually present as a more continuous boundary of disorder. The disordered boundaries of HAGBs in our system can be seen in the lower half portion of Fig. 5 (A and B) but are not formed by shear at the void interface. These HAGBs typically form as a result of larger grains merging during initial crystallization or cluster coalescence (22). Other points of disorder exist within the bulk crystal as well but are typically due to defects associated with the particles themselves, e.g., aggregated particles. Only dislocations that follow the boundary between misoriented grains are considered as being associated with a LAGB.

The formed LAGBs contain repeating 5,7 edge dislocations. The 5 and 7 in this case refer to the number of nearest neighbors of the particle pair that make up the dislocation. Figure 5C depicts a magnified view of the LAGBs, where particles with 7 nearest neighbors and those with 5 nearest neighbors are colored blue and magenta, respectively. Each dislocation along the LAGB that is marked by disorder via ψ_6 in Fig. 5B, corresponds to a 5,7 pair of particles in Fig. 5C. The lattice distortion is further highlighted in Fig. 5D, where a line of the lattice (magenta) terminates, resulting in an edge dislocation. The dislocation causes the surrounding lattice (white) to bend around the termination point. Modeling a grain boundary as an array of edge dislocations is one of the most common methods used to develop predictive theories in hard-condensed matter (48).

Application of Read-Shockley theory

Read and Shockley's LAGB theory is used to predict the misorientation angle and energy of the shear-induced LAGBs. Since the Read-Shockley theory assumes geometrical constraints characteristic of 2D systems, it is reasonable to apply it to our 2D system, beginning with the misorientation angle. The misorientation angle of a LAGB, composed of repeating edge dislocations, is related to the Burgers vector of the dislocations |b|, and the distance between neighboring dislocations, h, through the relationship

 $\theta_{mis} = \frac{|b|}{h} \tag{1}$

Since the shear-induced LAGBs in this system have the same repeating 5,7 edge dislocations, their structure satisfies the assumption of this relationship (Eq. 1) that all dislocations have identical magnitudes of their Burgers vector (|b|). As a result, the magnitudes of all Burgers vectors, measured via a Burgers circuit (Fig. 5E), are 1.2 μ m. This value is equivalent to the interparticle spacing, which is expected since it is a geometrical identity of colloidal and atomic crystals. Conversely, h (Fig. 5C) varies across each LAGB, so an average value was taken. This variability is present in hard-condensed matter, where grain boundaries are far from ideal (49.50).

The misorientation angles that were calculated from the LAGBs' dislocation structure are compared with angles experimentally measured on the lattice through θ_6 differences, shown in Table 1. Overall, the measured and calculated values for each LAGB are in good agreement. This agreement illustrates that our dynamic colloidal system generates LAGBs, whose misorientation angle can be deduced from the dislocation structure.

To extend this classical grain boundary theory to our soft matter system, the energy of the shear-induced LAGBs was estimated. Following the Read-Shockley theory, the energy of a LAGB is calculated based primarily on the misorientation angle (20).

$$E = E_0 \theta_{mis} \left(A - \ln(\theta_{mis}) \right) \tag{2}$$

Page 7 of 18

Here, E_0 depends on the asymmetry of the grain boundary and the bulk material's elastic constants, i.e., the rigidity modulus and Poisson's ratio, and A depends on the asymmetry of the grain boundary and the strain field caused by a single dislocation. E_0 is directly proportional to the rigidity modulus, making the energy of the grain boundary significantly depend on the value of the rigidity modulus used. Therefore, the rigidity modulus in this 2D colloidal sheet was determined through line tension measurements previously taken with this system (22). The other elastic constant, Poisson's ratio, was taken from literature that examined the elasticity of 2D colloidal crystals (51). While other colloidal crystal systems have reported slightly varied Poisson's ratio values (52), the variation is not enough to significantly influence the value of E. Therefore, an approximate value for our system was sufficient. All other variables were measured experimentally through image processing. Further details on the calculation of E can be found in Methods.

The Read-Shockley theory (Eq. 2) predicts energy values for the LAGBs in this system that range from $(2.05 \pm 0.07) \times 10^{-15}$ J/m to $(1.74 \pm 0.06) \times 10^{-15}$ J/m. The values are only one order of magnitude smaller than Wei and Wu (53), who estimated the energy of grain boundaries in colloidal crystals based on a probability density function. The discrepancy in magnitude is likely because our energy calculation is specific to LAGBs, while their calculation was general for a system that favored HAGB formation. LAGBs tend to have a lower energy than HAGBs so it follows that our values would be lower. With regard to 2D hard-condensed matter, LAGB energies are four or five orders of magnitude greater (2,54) than those found in this colloidal system. This greater discrepancy is expected since system differences, such as length scale, magnitude of the interaction potential, or LAGB variation, would all cause a mismatch in quantitative values. Ultimately, the energy values predicted by the Read-Shockley theory for our shear-induced LAGBs are within reason for a 2D colloidal crystal system.

These results report the effect of shear at the void-crystal interface of a 2D colloidal crystalline sheet. Interfacial shear was achieved by applying an in-plane rotating magnetic field to 2D colloidal sheets of superparamagnetic particles, creating a colloidal crystal bulk that contained particle-free voids. Unlike previous systems that have aimed to temporarily shear and/or rotate colloidal crystals, this system contains an inherent torque that drives the shear at the crystal-void interface, continuously rotating the crystalline bulk. This inherent torque could be used to better elucidate the role of internal and/or external shear on grain boundary movement during material processing. More specifically, the shear-induced grain rotation presents an ideal experimental setup to explore theorized mechanisms of grain boundary motion that have been difficult to observe experimentally, e.g., grain growth as a result of shear-coupled rotation (55). This colloidal system as an experimental model is further bolstered with the application of geometrically and energetically derived equations from Read and Shockley. Moreover, the ability to modulate particle interactions through the magnetic field, much like temperature in hardcondensed matter, makes this colloidal system ideal for studying the effects of annealing on grain boundaries. While this work makes no claim to produce quantitative results that match hard-condensed matter, it is an example of a system that despite being torquedriven, has promise to provide foundational knowledge for polycrystalline systems. These insights help close the gap between soft colloidal crystals and the hard-condensed matter systems they aim to model.

Materials and Methods

Colloidal suspension and sample chamber

The polystyrene particles used in this study have a mean diameter of 1.1 ± 0.08 µm and contain embedded iron-oxide nanoparticles that impart a volumetric magnetic susceptibility of 1.4 (Dynabeads MyOne Carboxylic Acid from Invitrogen). The particles' exterior carboxylic acid group provides a negative surface charge that inhibits aggregation, with a zeta potential of -40 mV. For this work, the particles were washed and dispersed in 10 mM NaCl (aqueous) to screen their electrostatic charges. This screening allows for tighter packing of the colloids into ordered sheets. Final suspension concentrations ranged from 3 to 4 mg/ml.

Following previously reported work (22), 40 μ l of the colloidal suspension was drawn between two plasma-cleaned glass cover slips (Ted Pella, Inc.) that were separated by a parafilm spacer, and the entire glass chamber was sealed with a fast-setting epoxy and UV-curable adhesive. Since the particles are denser than the fluid, the negative charge imparted to the glass cover slips during plasma-cleaning allowed the particles to settle to a quasi-2D layer just above the bottom of the chamber. The adhesives sealed the chamber such that evaporation was negligible over the course of an experiment. Each experiment was run with a new sample chamber and particle suspension.

Magnetic Field and sheet formation

Each sample was placed on a stage at the center of two pairs of solenoid coils, set orthogonal to one another, and connected to a power supply (Agilent N6784A). After allowing time for the particles to settle, individual particle resolution was achieved from below with a 100x Olympus objective. The objective lens was placed in line with a mirror that relayed the image to a camera (QICAM Fast 1394) and recordings were captured on SimplePCI imaging software.

To induce 2D ordering of the settled particles, a rotating magnetic field was produced in-plane by running sinusoidal waves, offset by 90 degrees, through the coil pairs. The field was rotated at a frequency of 20 Hz to create an isotropic interaction pair-potential between particles that was proportional to the inverse of the interparticle spacing cubed (r^{-3}) and scaled with the strength of the magnetic field squared (H^2) , following previous work (21). This procedure allows for the interparticle spacing (r) to be controlled by the strength of the magnetic field (H), meaning an increase/decrease in field strength will transition the system to a more ordered/disordered phase, respectively (29). For this work, a solid-like crystalline phase was achieved within the particle sheets with a relatively strong magnetic field of 1.15 mT. For each experiment, the field was first turned on to induce crystalline sheet formation, and then recording began. The particle sheets shown in this work were recorded for up to 3 hours, while the magnetic field was maintained at 1.15 mT. Particle surface area coverage ranged from 50 to 60 percent.

Grain Boundary Identification

Grain boundaries were identified by the quantification of order and orientation in the system, on a particle-by-particle basis, through the local bond-orientational order parameter ψ_6 and it's phase θ_6 , respectively. ψ_6 determines the degree of local hexagonal order in spherical particle systems and was used in the following form

$$\psi_6 = \frac{1}{N_n} \sum_k \exp i6\theta_k \tag{3}$$

Here, N_n corresponds to the number of nearest neighbors k to the particle of interest, determined through a Voronoi diagram, and θ_k is the angle made between the positive x-axis and the vector connecting the particle of interest to each of its neighbors, as previously shown in Fig. 1E. Particle centers were identified using in-house Matlab scripts, based on particle size and image intensity values. The value of ψ_6 ranges from 0 to 1, where 0 indicates disorder and 1 indicates hexatic order.

The local orientation, θ_6 , was calculated by taking the argument of ψ_6 , shown below

$$\theta_6 = arg(\psi_6) \tag{4}$$

Mathematically speaking, θ_6 is the angle on the complex plane between the positive real axis and a line connecting the origin to the ψ_6 value. However, in hexagonally ordered particle systems it is physically the local lattice orientation, measured against the positive x-axis, as shown previously in Fig. 1C. Since hexagonally ordered systems have six-fold symmetry, the value of θ_6 will never exceed 60° . The value of θ_6 varies across a crystal and is a result of thermal fluctuations in the crystal. For the purpose of grain boundary identification, an approximate overall crystal orientation was sufficient to identify misoriented crystals.

Grain boundaries were identified by having low ψ_6 values along a border that neighbored ordered grains whose θ_6 values did not match. The disordered borders were either connected lines of disorder or points of disorder that followed the boundary. High angle grain boundaries (HAGBs) presented as connected lines of disorder, while low angle grain boundaries (LAGBs) presented as discrete regions of disorder along the boundary (Fig. 1, C and D).

The fraction of particles found within a grain boundary, x_{GB} , was used to quantify global changes in order with time. This value was estimated on a per frame basis by taking the number of particles with a $\psi_6 \le 0.4$ and dividing it by the total number of particles found. This cut off value of 0.4 was chosen on the basis that grain boundaries are made up predominantly of $^{\psi_6}$ values from 0 to approximately 0.4 and higher middle-range $^{\psi_6}$ values can be found occasionally throughout the bulk crystal due to small thermal fluctuations but are not a part of the grain boundaries. Therefore, using this cutoff value decreased the amount of noise in the data, while still containing the majority of the particles in the grain boundary. The remaining noise was due to small particle defects, e.g., aggregates, or momentary changes in focus. To remove the noise, each $^{X}_{GB}$ data set was filtered to remove outliers and a moving average was applied. Outliers were taken as any value that deviated from the local mean by more than two standard deviations. The local mean was computed by averaging 500 nearest neighbors in time on either side of the data point of interest. The moving average was taken over 80 points and the standard deviation of the moving average was computed, shown as gray shading in $^{X}_{GB}$ plots.

The probability of θ_6 with time was used to quantify global orientational changes with time, depicted as a color plot, for the purpose of highlighting annihilation and formation. A normalized histogram with 61 bins was created from the θ_6 values found per frame, where each bin corresponded to a particular degree from 0° to 60° . The normalized height of each bin was taken as the probability. The 61 bins were then plotted with time, where the color of the plot corresponds to the probability of each θ_6 value occurring at that point in time.

Misorientation angle calculations

The misorientation angle θ_{mis} quantifies the difference in orientation between crystal grains that are separated by a grain boundary. θ_{mis} of the shear-induced LAGBs was calculated by two different methods to arrive at an experimentally measured value and a calculated value.

Experimental θ_{mis} Value

Due to the variation in θ_6 across a crystal, the experimentally observed misorientation angle was obtained by directly measuring the difference in lattice orientation across the grain boundary. This measurement was taken with ImageJ atop the microscopy images, as shown previously in Fig. 5A. Forty measurements were taken along each grain boundary and then averaged to arrive at a single misorientation angle for each LAGB. Minor fluctuations in values were found across the grain boundaries but error remained low, never exceeding 6% for all LAGBs measured.

Read-Shockley θ_{mis} Value

To calculate θ_{mis} based on each LAGB's dislocation structure, the relationship from Read and Shockley (20) was used (Eq. 1). To determine the magnitude of the Burgers vector (|b|) and the spacing between dislocations (h), the dislocations were first identified explicitly. This identification was done by color coating the 5,7 particle pair that made up the dislocation on the microscopy images, as shown previously in Fig. 5C. 5 and 7 refer to the number of nearest neighbors each particle in the pair has, colored magenta and blue, respectively.

Page 10 of 18

The Burgers vector magnitude |b| was determined by drawing a Burgers circuit around each colored dislocation, as depicted in Fig. 5E. As per a Burgers circuit, all four sides of the rectangular path traversed the same number of particles along the lattice but failed to start where it began, quantifying the lattice distortion. The Burgers vector is defined as the vector that closes this path. For this system, all LAGBs are made of up of identical 5,7 edge dislocations for which the magnitude of the Burgers vector is simply the interparticle spacing. Therefore, a Matlab code was used to obtain a precise interparticle spacing by identifying particle centers via image intensity values. Since thermal fluctuations cause variation in this value, multiple measurements were taken from Matlab and averaged to give a single interparticle spacing for the colloidal crystalline bulk. The value of 1.2 μ m that was found for |b| was applied to all LAGBs. Error was low at a value of 0.75%.

The spacing between dislocations h is specific to each LAGB and was therefore measured per LAGB. This measurement was taken via ImageJ atop the microscopy images that were color coated for the 5,7 edge dislocations, as shown in Fig. 5C. h was taken as the average of the shortest distance between adjacent dislocations, measuring off of the particle with 5 nearest neighbors. Each adiacent dislocation was again measured multiple times to reduce the error in measurement. All LAGBs had an associated error of no more than 0.5% for their corresponding h value.

Estimation of Grain Boundary Energy

68 69

70

71 72

73

74 75

76

77

78 79

80

81

82 83

84

85

86

87

88 89 90

91

92

93

94 95

96

97

99

00

01

02

03

04

05

06

07

09 10 The grain boundary energy was calculated for the shear-induced LAGBs by direct application of the energy equation theorized by Read and Shockley (20), which relates the energy of a grain boundary directly to its misorientation angle, θ_{mis} (see Eq. 2). E_0 and Ain Eq. 2 are varying functions of ϕ , the orientation of the grain boundary, and are shown below.

$$E_0 = \frac{Ga}{4\pi(1-\sigma)}(\cos\phi + \sin\phi) \tag{5}$$

$$E_0 = \frac{Ga}{4\pi (1 - \sigma)} (\cos\phi + \sin\phi)$$

$$A = 1 + \ln\left[\frac{a}{2\pi r_0}\right] - \frac{\sin(2\phi)}{2} - \frac{\sinh(\sin\phi) + \cos\phi\ln(\cos\phi)}{\sin\phi + \cos\phi}$$
(6)

In these secondary equations, G is the rigidity modulus of the bulk material, a is the lattice spacing, σ is Poisson's ratio, and r_0 is the radial distance of strain caused by a dislocation.

The rigidity modulus G of the colloidal crystal system was taken as the line tension of the colloidal crystal system at 1.15 mT, divided by the particle diameter, giving the appropriate 2D units of J/m^2 . Line tension measurements were taken from our previous work (22). Poisson's ratio was taken from 2D literature that had probed colloidal crystal elasticity (51). Others have reported varying Poisson ratio values (52), but the variation found in the literature did not significantly change the calculated energy value.

The remaining variables: a, r_0 , and ϕ were all experimentally measured, either on a system-wide basis or LAGB basis. Since the lattice spacing does not change in the bulk for a constant field strength, barring small fluctuations, a was measured on a system-wide basis via Matlab image analysis. This value is the same value calculated for the magnitude of the Burgers vector above and was taken from the bulk, i.e., not near the void interface where fluctuations are greater.

The strain field, r_0 , was also determined on a system-wide basis since all LAGBs contained the same type of 5,7 edge dislocation and therefore should have similar strain fields associated with their formation. r_0 was determined by measuring the radial distance out from a dislocation for which ψ_6 was approximately less than 1 (see fig. S1). This measurement rests on the assumption that the lattice is strained only in the vicinity for which disorder occurs. All 5,7 edge dislocations in the formed LAGBs were measured and averaged to arrive at a single r_0 value. While there was some variation, a low error of 2.6% was obtained.

The orientation of each LAGB ϕ was found by measuring the orientation of each neighboring grain with respect to the grain boundary, ϕ_1 and ϕ_2 , (fig. S1) and computing the difference between the two angles. If the lattice on either side approached the grain boundary with the same angle, ϕ was equal to zero and the grain boundary was considered symmetric. Both symmetric and asymmetric grain boundaries formed in this system. The grain boundary line was determined by drawing a straight line through the dislocations. If there was a fluctuation on the grain boundary, e.g., a step, another line with the same orientation was drawn through the remaining dislocations to guarantee that ϕ_1 and ϕ_2 were measured off of the same grain boundary line. This double line is elucidated in fig. S1. Forty-five measurements were taken for both ϕ_1 and ϕ_2 and then averaged to arrive at a single difference value. All LAGBs had low error associated with their measured ϕ values, never exceeding 5%.

References

- 1. N. Hansen, Hall-Petch relation and boundary strengthening. Scripta Materialia. 51, 801-806 (2004).
- 2. O. V. Yazyev, Y. P. Chen, Polycrystalline graphene and other two-dimensional materials. *Nat. Nanotechnol.* **9**, 755-767, (2014).
- 3. X. Zhang, J. Han, J. J. Plombon, A. P. Sutton, D. J. Srolovitz, J. J. Boland, Nanocrystalline copper films are never flat. *Science*. **357**, 397-400 (2017).
- 4. L. Priester, Grain Boundaries: From Theory to Engineering (Springer, Dordrecht, ed. 2013th edition, 2012).
- 5. J. W. Cahn, Y. Mishin, A. Suzuki, Coupling grain boundary motion to shear deformation. *Acta Mater.* **54**, 4953-4975 (2006).
- 6. M. Winning, G. Gottstein, L. S. Shvindlerman, Migration of grain boundaries under the influence of an external shear stress. *Mater. Sci. Eng.*, A. **317**, 17-20 (2001).
- 7. T. Gorkaya, K. D. Molodov, D. A. Molodov, G. Gottstein, Concurrent grain boundary motion and grain rotation under an applied stress. *Acta Mater.* **59**, 5674-5680 (2011).
- 8. B. Li, D. Zhou, Y. Han, Assembly and phase transitions of colloidal crystals. *Nat. Rev. Mater.* **1**, 15011 (2016).
- 9. T. O. E. Skinner, D. G. A. L. Aarts, R. P. A. Dullens, Grain-Boundary Fluctuations in Two-Dimensional Colloidal Crystals. *Phys. Rev. Lett.* **105**, 168301 (2010).
- 10. F. A. Lavergne, D. G.A.L. Aarts, R. P.A. Dullens, Anomalous Grain Growth in a Polycrystalline Monolayer of Colloidal Hard Spheres. *Phys. Rev. X.* 7, 041064 (2017).
- 11. M. Liao, X. Xiao, S. T. Chui, Y. Han, Grain-Boundary Roughening in Colloidal Crystals. *Phys. Rev. X.* **8**, 021045 (2018).
- 12. K. H. Nagamanasa, S. Gokhale, R. Ganapathy, A. K. Sood, Confined glassy dynamics at grain boundaries in colloidal crystals. *Proc. Natl. Acad. Sci.* **108**, 11323-11326 (2011).
- 13. F. A. Lavergne, A. Curran, D. G. A. L. Aarts, R. P. A. Dullens, Dislocation-controlled formation and kinetics of grain boundary loops in two-dimensional crystals. *Proc. Natl. Acad. Sci.* **115**, 6922-6927 (2018).
- 14. C. E. Cash, J. Wang, M. M. Martirossyan, B. K. Ludlow, A. E. Baptista, N. M. Brown, E. J. Weissler, J. Abacousnac, S. J. Gerbode, Local Melting Attracts Grain Boundaries in Colloidal Polycrystals. *Phys. Rev. Lett.* **120**, 018002 (2018).
- 15. W. T. M. Irvine, A. D. Hollingsworth, D. G. Grier, P. M. Chaikin, Dislocation reactions, grain boundaries, and irreversibility in two-dimensional lattices using topological tweezers. *Proc. Natl. Acad. Sci.* **110**, 15544-15548 (2013).

Science Advances Manuscript Template Page 12 of 18

- 16. B. van der Meera, W. Qi, R. G. Fokkink, J. van der Gucht, M. Dijkstra, J. Sprakel, Highly cooperative stress relaxation in two-dimensional soft colloidal crystals. *Proc. Natl. Acad. Sci.* **111**, 15356–15361 (2014).
 - 17. W. Li, Y. Peng, Y. Zhang, T. Still, A. G. Yodh, Y. Han. Shear-assisted grain coarsening in colloidal polycrystals. *Proc. Natl. Acad. Sci.* **117**, 24055-24060 (2020).

- S. Gokhale, K. H. Nagamanasa, V. Santhosh, A. K. Sood, R. Ganapathy, Directional grain growth from anisotropic kinetic roughening of grain boundaries in sheared colloidal crystals. *Proc. Natl. Acad. Sci.* 109, 20314–20319 (2012).
- 19. I. Buttinoni, M. Steinacher, H. Th. Spanke, J. Pokki, S. Bahmann, B. Nelson, G. Foffi, L. Isa1, Colloidal polycrystalline monolayers under oscillatory shear. *Phys. Rev. E.* **95**, 012610 (2017).
- 20. W. T. Read, W. Shockley, Dislocation Models of Crystal Grain Boundaries. Phys. Rev. 78, 275-289 (1950).
- 21. D. Du, D. Li, M. Thakur, S. L. Biswal, Generating an in situ tunable interaction potential for probing 2-D colloidal phase behavior. *Soft Matter.* **9**, 6867 (2013).
- 22. E. Hilou, D. Du, S. Kuei, S. L. Biswal, Interfacial energetics of two-dimensional colloidal clusters generated with a tunable anharmonic interaction potential. *Phys. Rev. Mater.* **2**, 025602 (2018).
- 23. S. Jäger, H. Stark, S. H. L. Klapp, Dynamics of cluster formation in driven magnetic colloids dispersed on a monolayer. *J. Phys.: Condens. Matter.* **25**, 195104 (2013).
- 24. J. E. Martin, A. Snezhko, Driving self assembly and emergent dynamics in colloidal suspensions by time-dependent magnetic fields. *Rep. Prog. Phys.* **76**, 126601 (2013).
- 25. S. H. L. Klapp, Collective dynamics of dipolar and multipolar colloids: From passive to active systems. *Curr. Opin. in Colloid Interface Sci.* **21**, 76-85 (2016).
- 26. A. T. Pham, Y. Zhuang, P. Detwiler, J. E. S. Socolar, P. Charbonneau, B. B. Yellen, Phase diagram and aggregation dynamics of a monolayer of paramagnetic colloids. *Phys. Rev. E.* **95**, 052607 (2017).
- 27. K. A. Komarov, S. O. Yurchenko, Colloids in rotating electric and magnetic fields: designing tunable interactions with spatial field hodographs. *Soft Matter.* **16**, 8155-8168 (2020).
- 28. N. Elsner, C. P. Royall, B. Vincent, D. R. E. Snoswell, Simple models for two-dimensional tunable colloidal crystals in rotating ac electric fields. *J. Chem. Phys.* **130**, 154901 (2009).
- 29. D. Du, M. Doxastakis, E. Hilou, S. L. Biswal, Two-dimensional melting of colloids with long-range attractive interactions. *Soft Matter.* **13**, 1548-1553 (2017).
- 30. A. S. Salazar, D. M. Lobmeyer, L. H. P. Cunha, K. Joshi, S. L. Biswal, Hierarchical assemblies of superparamagnetic colloids in time-varying magnetic fields. *Soft Matter*. **17**, 1120-1155 (2021).
- 31. E. Hilou, K. Joshi, S. L. Biswal, Characterizing the spatiotemporal evolution of paramagnetic colloids in time-varying magnetic fields with Minkowski functionals. *Soft Matter.* **16**, 8799-8805 (2020).
- 32. X. J. A. Janssen, A. J. Schellekens, K. van Ommering, L. J. van IJzendoorn, M. W. J. Prins, Controlled torque on superparamagnetic beads for functional biosensors. *Biosens. Bioelectron.* 24, 1937-1941 (2009).
- 33. P. Tierno, R. Muruganathan, T. M. Fischer, Viscoelasticity of Dynamically Self-Assembled Paramagnetic Colloidal Clusters. *Phys. Rev. Lett.* **98**, 028301 (2007).
- M. M. van Oene, L. E. Dickinson, F. Pedaci, M. Köber, D. Dulin, J. Lipfert, N. H. Dekker, Biological Magnetometry: Torque on Superparamagnetic Beads in Magnetic Fields. *Phys. Rev. Lett.* 114, 218301 (2015).
- 35. H. Massana-Cid, F. Meng, D. Matsunaga, R. Golestanian, P. Tierno, Tunable self-healing of magnetically propelling colloidal carpets. *Nat. Commun.* **10**, 2444 (2019).
- 36. F. Martinez-Pedrero, P. Tierno, Magnetic Propulsion of Self-Assembled Colloidal Carpets: Efficient Cargo Transport via a Conveyor-Belt Effect. *Phys. Rev. Appl.* **3**, 051003 (2015).
- 37. T. O. Tasci, P. S. Herson, K. B. Neeves, D. W. M. Marr, Surface-enabled propulsion and control of colloidal microwheels. *Nat. Commun.* **7**, 10225 (2016).
- 38. E. S. Bililign, F. B. Usabiaga, Y. A. Ganan, A. Poncet, V. Soni, S. Magkiriadou, M. J. Shelley, D. Bartolo, and W. T. Irvine, Motile dislocations knead odd crystals into whorls. *Nat. Phys.* **18**, 212-218 (2022).
- 39. T. H. Tan, A. Mietke, H. Higinbotham, J. Li, Y. Chen, P. J. Foster, S. Gokhale, J. Dunkel, N. Fakhri, Development drives dynamics of living chiral crystals. arXiv:2105.07507 [cond-mat.soft] (2021).
- 40. V. Soni, E. S. Bililign, S. Magkiriadou, S Sacanna, D. Bartolo, M. J. Shelley, W. T. Irvine, The odd free surface flows of a colloidal chiral fluid. *Nat. Phys.* **15**, 1188-1194 (2019).
- 41. P. Tierno, A. Snezhko, Transport and Assembly of Magnetic Surface Rotors, *Chem. Nano. Mat.* 7, 881-893 (2021).
- 42. J. Yan, S. C. Bae, S. Granick, Rotating crystals of magnetic Janus colloids. Soft Matter. 11, 147-153 (2015).
- 43. A. J. Haslam, D. Moldovan, V. Yamakov, D. Wolf, S. R. Phillpot, H. Gleiter, Stress-enhanced grain growth in a nanocrystalline material by molecular-dynamics simulation. *Acta Mater.* **51**, 2097-2112 (2003).
- 44. G. Gottstein, *Physical Foundations of Materials Science* (Springer-Verlag, Berlin Heidelberg, 2004).
- 45. A. Azizi, X. Zou, P. Ercius, Z. Zhang, A. L. Elías, N. Perea-López, G. Stone, M. Terrones, B. I. Yakobson, and N. Alem, Dislocation motion and grain boundary migration in two dimensional tungsten disulphide.
 Nat. Commun. 5, 4867 (2014).

Science Advances Manuscript Template Page 13 of 18

- 46. Q. Zhu, Q. Huang, C. Guang, X. An, S. X. Mao, W. Yang, Z. Zhang, H. Gao, H. Zhou, J. Wang, Metallic nanocrystals with low angle grain boundary for controllable plastic reversibility. *Nat. Commun.* **11**, 3100 (2020).
 - 47. J. T. Kindt, Competing factors in grain boundary loop shrinkage: Two-dimensional hard sphere colloidal crystals. *J. Chem. Phys.* **151**, 084505 (2019).
 - 48. J. Han, S. L. Thomas, D. J. Srolovitz, Grain-boundary kinetics: A unified approach. *Prog. Mater. Sci.* **98**, 386-476 (2018).
 - 49. L. Priester, Grain Boundaries and Crystalline Plasticity (John Wiley & Sons, 2013).
 - 50. C. L. Johnson, M. J. Hÿtch, P. R. Buseck, Nanoscale waviness of low-angle grain boundaries. *Proc. Natl. Acad. Sci.* **101**, 17936-17939 (2004).
 - 51. W. Lechner, C. Dellago, Point defects in two-dimensional colloidal crystals: simulation vs. elasticity theory. *Soft Matter.* **5**, 646-659 (2009).
 - 52. J. Zanghellini, P. Keim, H. H. von Grünberg, The softening of two-dimensional colloidal crystals. *J. Phys.: Condens. Matter.* 17, S3579-S3586 (2005).
 - 53. Q. H. Wei, X. L. Wu, Grain boundary dynamics under mechanical annealing in two-dimensional colloids. *Phys. Rev. E.* **70**, 020401 (2004).
 - 54. Z. G. Yu, Y. W. Zhang, B. I. Yakobson, An Anomalous Formation Pathway for Dislocation-Sulfur Vacancy Complexes in Polycrystalline Monolayer MoS2. *Nano Lett.* **15**, 6855-6861 (2015).
 - 55. J. W. Cahn, J. E. Taylor, A unified approach to motion of grain boundaries, relative tangential translation along grain boundaries, and grain rotation. *Acta Mater.* **52**, 4887-4898 (2004).

Acknowledgments

 We thank Zachary Cordero and Logan Ware for helpful discussions regarding LAGBs. We also thank Elaa Hilou and Dylan Jurski for their assistance in conducting experiments and writing Matlab scripts, respectively.

Funding: This material is based upon work supported by the National Science Foundation under Grant No. CBET-1705703.

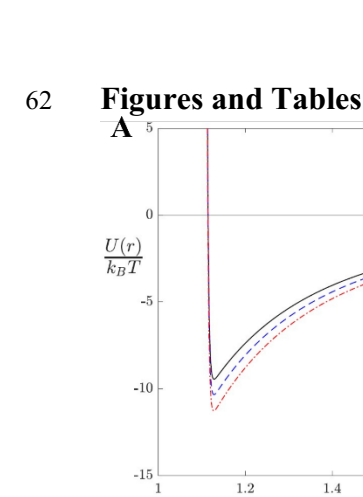
Author contributions: D.M.L performed the experiments and calculations under the guidance of S.L.B. S.L.B and D.M.L. wrote the manuscript.

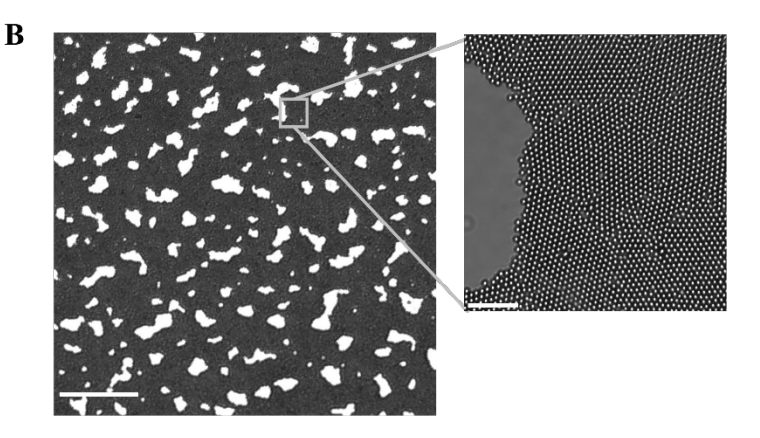
Competing interests: The authors declare that they have no competing interests.

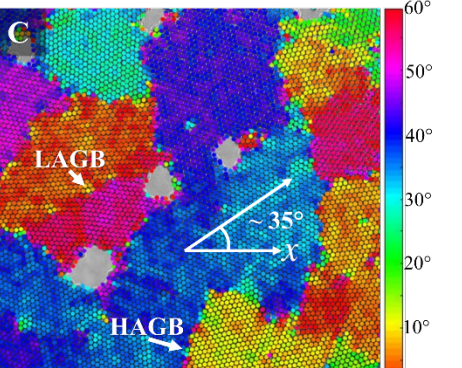
Data and materials availability: The data for this work have been deposited in the Rice Digital Scholarship Archive (https://doi.org/10.25611/740B-YR87).

Page 14 of 18

Science Advances Manuscript Template





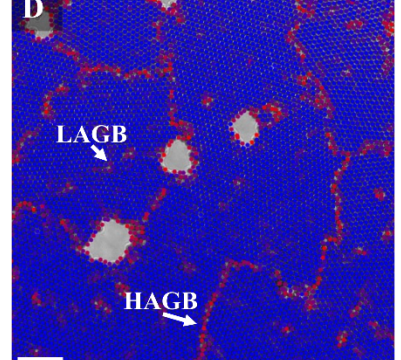


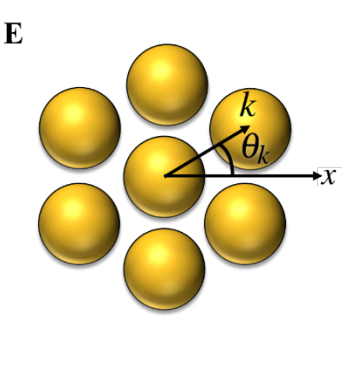
1.6

 $r(\mu m)$

1.8

-1.10 mT -1.15 mT -1.20 mT





63 64 65 66 67 68 69 70 71 72

73

74

Fig. 1. Magnetic field induced polycrystalline sheet formation. (A) Particles interact isotopically in-plane according to the tunable interaction pair-potential (U(r)), normalized with k_BT , where r is the interparticle spacing. The schematic depicts this interaction on a pair of negatively charged particles with rotating dipoles. (B) Immediately upon application of a RMF, paramagnetic particles assemble into particle dense regions (black), leaving behind particle-free voids (white). Scale bar, 100 μm. The inset is a close up of the bulk-void interface. Scale bar, 10 μm. (C) Crystalline grains with distinct grain boundaries form in the bulk, as shown by an overlaid colormap of the local orientation, θ_6 , and (D) the local bond-orientational order parameter, ψ_6 . Low angle grain boundaries (LAGB) contain borders of discrete disorder, while high angle grain boundaries (HAGB) have continuous disorder. Scale bars, 10 μm. (E) Angle θ_k used to calculate ψ_6 and subsequently θ_6 .

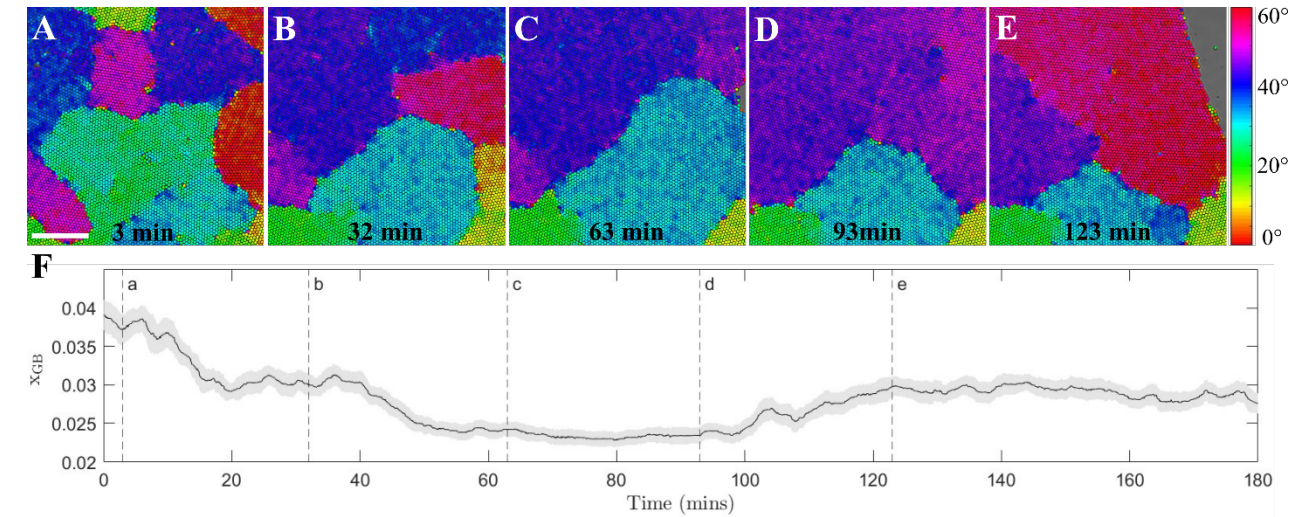


Fig. 2. Polycrystalline Bulk Evolution. (A) Many crystals form initially and (B to D) then combine and reorganize to less, reducing the number of grain boundaries temporarily, (E) until new grain boundaries form near a void. Times stamps indicate time since RMF has been turned on. Microscopy images are overlaid with a θ_6 colormap. Scale bar, 20 µm. (F) The changes in crystalline order are reflected in the decrease, and later increase, in the fraction of particles residing in grain boundaries, x_{GB} . Shading indicates standard deviation from the moving average.

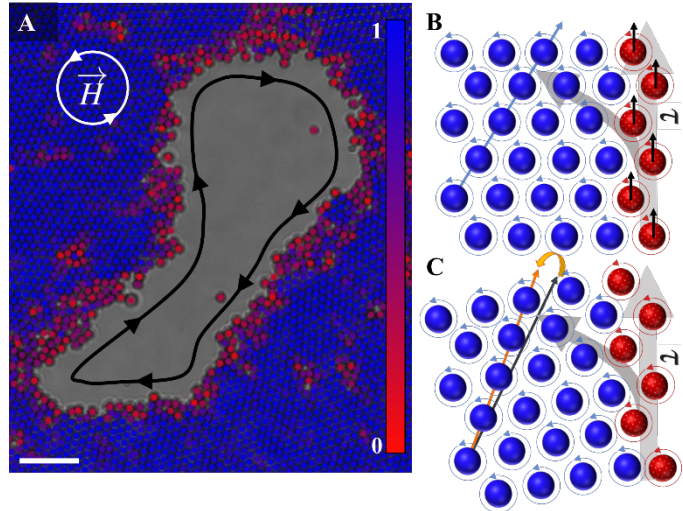


Fig. 3. Circulation-induced Shear. (A) At the crystal-void interface, a magnetic-field induced circulation arises in the opposite direction of field rotation, as a result of individual particle rotation. The disordered interface is highlighted by a ψ_6 colormap. Scale bar, 10 μ m. (B) Circulating particles at the interface produce a shearing force on the nearby bulk (C) that drives crystalline rotation.

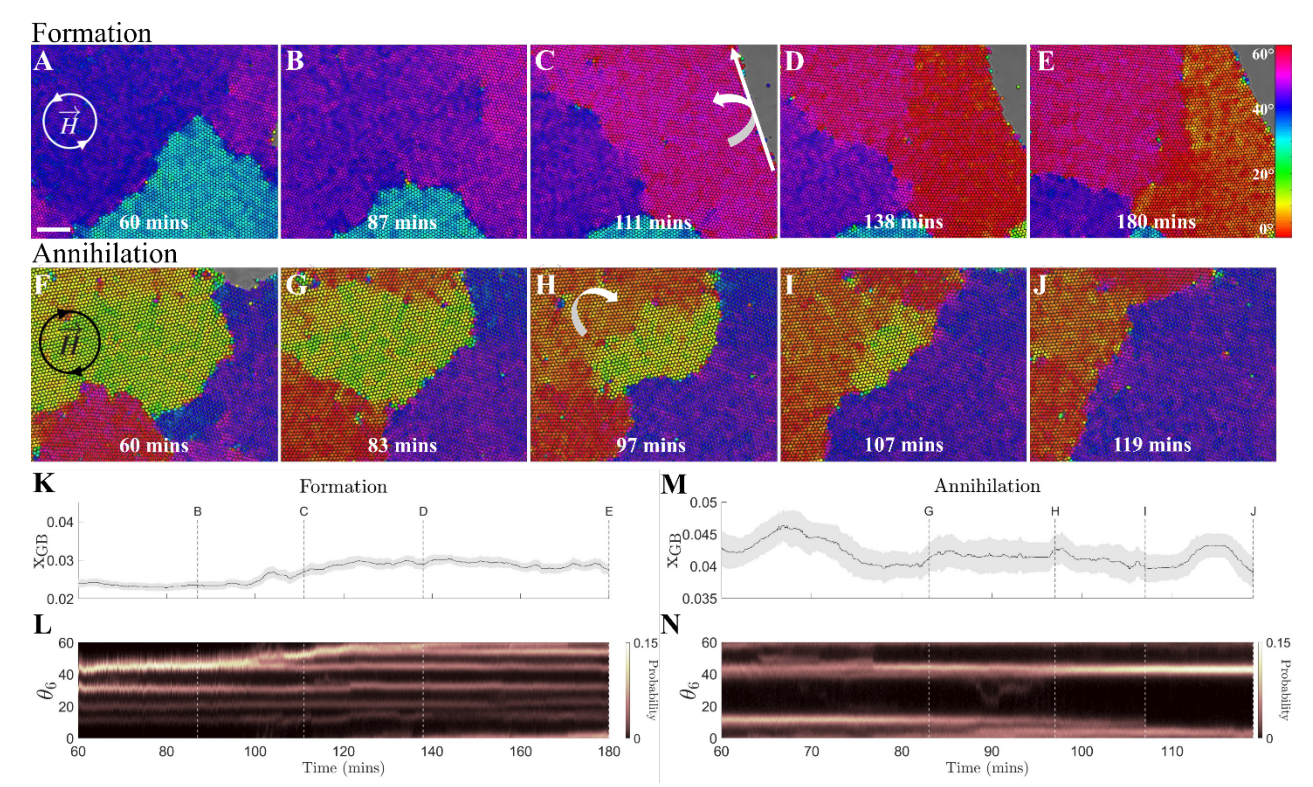


Fig. 4. Shear-induced grain rotation can both form and annihilate grain boundaries. (A to E) New grain boundaries form near a void (upper-right). (F to J) A large grain shrinks with time as the crystalline bulk is rotated from above. RMF direction shown atop first image in sequence. Time stamps indicate time since the RMF has been turned on. Microscopy images are overlaid with a θ₆ colormap. Scale bar, 10 μm. (K, L) Quantification of grain boundary formation. (K) The fraction of particles residing in grain boundaries, x_{GB}, increases, indicating an increase in grain boundaries, while (L) the measured probability distribution of θ₆ branches off, indicating an increase in the number of grains. (M, N) Quantification of grain boundary annihilation. As the grain boundary is annihilated, (M) x_{GB} decreases, and (N) the probability distribution of θ₆ narrows. More specifically, the probability around 10° disappears, indicating the complete removal of the grain.

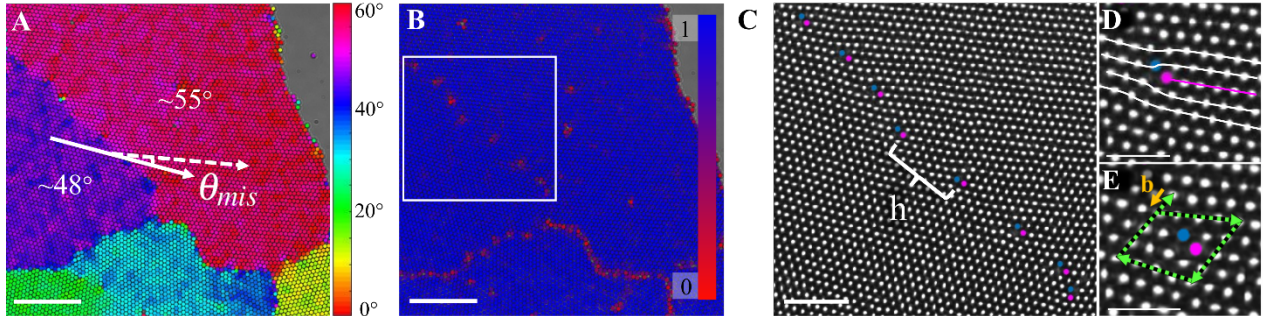


Fig. 5. Shear-induced low angle grain boundary structure. (A) An overlaid θ_6 colormap of a formed grain boundary indicates the formation of a LAGB ($\theta_{mis} \le 15^{\circ}$). Scale bar, 20 μm. (B) The LAGB (boxed in white) is composed of isolated points of disorder, as indicated by the overlaid ψ_6 colormap. Scale bar, 20 μm. (C) The magnified grain boundary's dislocations present as 5 (magenta), 7 (blue) dislocation pairs spaced a distance h from one another, 5 and 7 refer to the number of nearest neighbors a particle has, 6 being hexatic ordering. Scale bar, 10 μm. (D) A single 5,7 pair highlights the typical edge dislocation (magenta line) nature of these isolated pairs, and the resulting lattice distortion in one direction (white line). Scale bar, 5 μm. (E) An example of a Burgers circuit drawn around a dislocation (green dotted arrow) is used to highlight the Burgers vector (solid yellow arrow). Scale bars, 5 μm.

LAGB	$\theta_{\rm mis}$ Measured (°)	$\theta_{\rm mis}$ Calculated* (°)
1	8.625 ± 0.554	8.245 ± 0.030
2	6.758 ± 0.247	6.957 ± 0.022
3	10.253 ± 0.699	10.927 ± 0.036

Table 1. Experimentally measured and calculated θ_{mis} of shear-induced LAGBs.

Supplementary Materials

fig. S1

Movie S1

^{*} Using Eq. 1



Supplementary Materials for

Grain boundary dynamics driven by magnetically induced circulation at the void interface of 2D colloidal crystals

Dana M. Lobmeyer, Sibani L. Biswal*

*Corresponding author. Email: biswal@rice.edu

This PDF file includes:

Fig. S1 Legend for Movie S1

Other Supplementary Materials for this manuscript include the following:

Movie S1

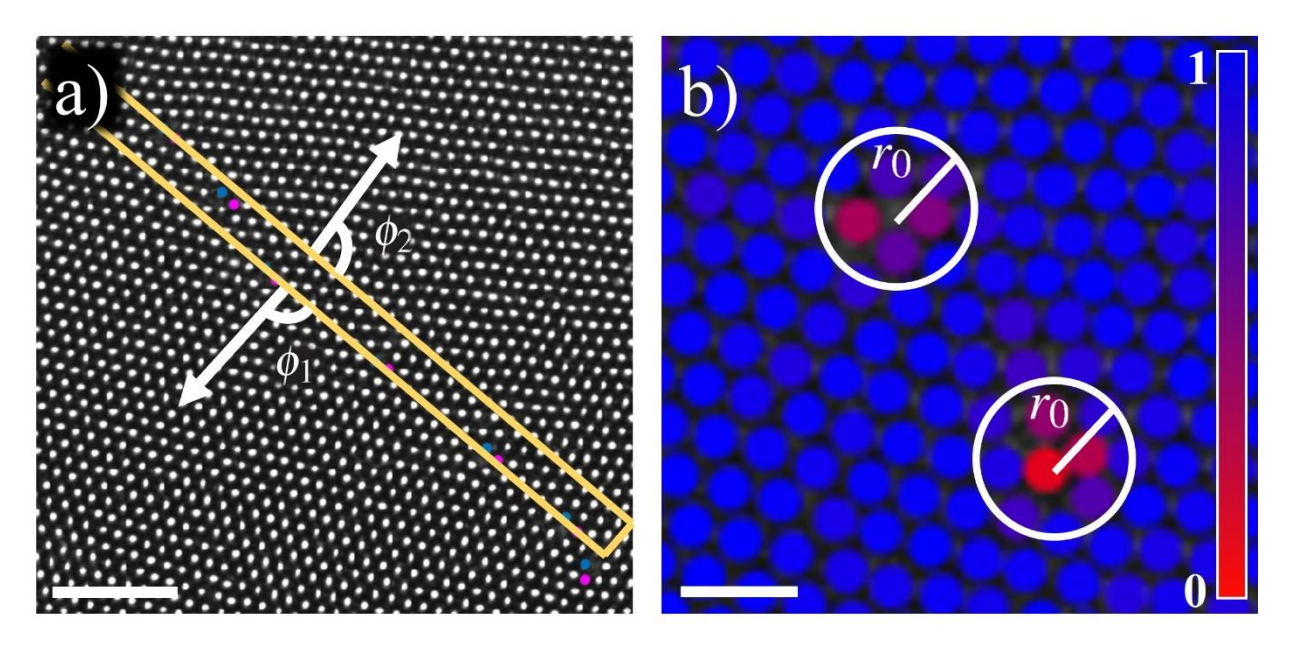


fig. S1. Visualization of r_0 **and** ϕ **variables** (a) Depiction of the variables used to calculate the orientation of the grain boundary ϕ . Note, the measurement requires a double line for the grain boundary since the boundary has a step in it. Scale bar, 10 µm. (b) Identification of the measured strain field r_0 of the 5,7 edge dislocations, highlighted by a ψ_6 color map. The circle encloses ψ_6 values less than approximately 1. Scale bar, 3 µm.

Movie S1. – Particle circulation at the crystal-void interface.

An aggregate of particles rotates around the void. The aggregate begins in the lower left corner of the video and is picked up by the movement along the edge of the void. It then continues in a clockwise path around the void, showcasing the circulatory motion at the crystal-void interface.